PNAS RESEARCH ARTICLE | ENGINEERING
APPLIED BIOLOGICAL SCIENCES

A closed-loop modular multiorgan-on-chips platform for self-sustaining and tightly controlled oxygenation

Nan Jiang[a,b,1,2], Guoliang Ying[a,1,2], Yixia Yin[a,1], Jie Guo[a,1], Jorge Lozada[a], Alejandra Valdivia Padilla[a], Ameyalli Gómez[a], Bruna Alice Gomes de Melo[a], Francisco Lugo Mestre[a], Merel Gansevoort[a], Marcello Palumbo[a], Noemi Calá[a], Carlos Ezio Garciamendez-Mijares[a], Ge-Ah Kim[c], Shuichi Takayama[c], Marie Denis Gerhard-Herman[d], and Yu Shrike Zhang[a,e,f,3]

Affiliations are included on p. 11.

Edited by Roger D. Kamm, Massachusetts Institute of Technology, Cambridge, MA; received July 15, 2024; accepted October 7, 2024 by Editorial Board Member John A. Rogers

To mimic physiological microenvironments in organ-on-a-chip systems, physiologically relevant parameters are required to precisely access drug metabolism. Oxygen level is a critical microenvironmental parameter to maintain cellular or tissue functions and modulate their behaviors. Current organ-on-a-chip setups are oftentimes subjected to the ambient incubator oxygen level at 21%, which is higher than most if not all physiological oxygen concentrations. Additionally, the physiological oxygen level in each tissue is different ranging from 0.5 to 13%. Here, a closed-loop modular multiorgan-on-chips platform is developed to enable not only real-time monitoring of the oxygen levels but, more importantly, tight control of them in the range of 4 to 20% across each connected microtissue-on-a-chip in the circulatory culture medium. This platform, which consists of microfluidic oxygen scavenger(s), an oxygen generator, a monitoring/controller system, and bioreactor(s), allows for independent, precise upregulation and downregulation of dissolved oxygen in the perfused culture medium to meet the physiological oxygen level in each modular microtissue compartment, as needed. Furthermore, drug studies using the platform demonstrate that the oxygen level affects drug metabolism in the parallelly connected liver, kidney, and arterial vessel microtissues without organ–organ interactions factored in. Overall, this platform can promote the performances of organ-on-a-chip devices in drug screening by providing more physiologically relevant and independently adjustable oxygen microenvironments for desired organ types on a single- or a multiorgan-on-chip(s) configuration.

oxygen control | thermoplastic chip | organ-on-a-chip | closed-loop platform | drug screening

Significance

Cellular and tissue functions are subjected to physiologically relevant microenvironmental oxygen levels. Current organ-on-a-chip platforms are supplemented with standard culture media beyond physiological oxygenation or ambient oxygen concentration in conventional hypoxia incubators, both failing to create the normoxic but oftentimes differential microenvironments for diverse microtissues of interest. Here, we describe the development of a closed-loop modular multiorgan-on-chips system that can tightly and independently control oxygen level for each desired organ type in the corresponding medium branch on a single platform. It is anticipated that the developed platform can significantly broaden the applications of multiorgan-on-chips models in disease modeling and drug screening with improved accuracy.

Maintenance of metabolic activities and functional behaviors of human tissues in vitro is critical for effective drug discovery and screening (1–4). Conventional two-dimensional (2D) or three-dimensional (3D) cell cultures have offered possibilities that enable cell survival in vitro (3, 5). However, the static cell culture, unlike dynamic microfluidic cell culture (6), is often limited by insufficient ability of continuous supply of fresh culture medium and fails to accurately reproduce the native microenvironments. An organ-on-a-chip platform allows for mimicking the 3D or compartmentalized organ-level functions of human physiology or diseases in vitro (7–10). With this platform, multiple miniature 3D microscale organs can also be fluidically linked for incorporation of interactional studies (11). As such, the organ-on-a-chip systems have been widely adopted as a class of powerful in vitro models for drug development and therapeutics screening (12).

Of note, oxygen level is essential to organs or tissues, as it is required for basic cellular functions (13). It is known that typical cell culture is performed at 21% of oxygen conditions (14), although levels that the cells experience in vivo are almost always far less than 21%, or ~160 mmHg. As a matter of fact, exposure to hyperoxic environments may affect metabolic activities, and even cause death to the cultured cells or microtissues by the formation of reactive oxygen species (15, 16). For example, oligodendrocyte progenitor cells used for the treatment of demyelinating diseases are ideally cultured at a lower oxygen level (5%) for expansion (17). It has also been proven that oxygen at the lower level could extend the lifespan of human diploid cells, while the cells do not proliferate in standard culture medium at the oxygen level of 21% (18). Besides, cancer cells rapidly outgrow in hypoxia, and as a result, studying tumor behaviors under controlled hypoxic conditions is important in improving the pathophysiology of a tumor-on-a-chip (19). Hypoxic conditions also possess a major impact on microtissue metabolisms, physiological pathways, and tissue remodeling (20). Hypoxia may inhibit or prevent the proliferation and growth of tissue cells in vitro, and it could be insufficient to maintain the respiration rate and the cells would presumably

This article is a PNAS Direct Submission R.D.K. is a guest editor invited by the Editorial Board.

[1]N.J., G.Y., Y.Y., and J.G. contributed equally to this work.

[2]Present address: Institute of Biomedical Engineering, West China School of Basic Medical Sciences and Forensic Medicine, Sichuan University, Chengdu 610041, People's Republic of China.

[3]To whom correspondence may be addressed. Email: yszhang@bwh.harvard.edu.

This article contains supporting information online at https://www.pnas.org/lookup/suppl/doi:10.1073/pnas.2413684121/-/DCSupplemental.

Published November 14, 2024.

obtain more of their energy from glycolysis (21). Therefore, it is of great importance to create oxygen-controlled environments in vitro pertaining to the in vivo conditions (18).

Furthermore, the physiological oxygen levels in the human body vary from organ to organ (Fig. 1*A*). Studies have investigated the typical oxygen levels in the main organs, such as 10 to 13% in the arterial blood, 0.5 to 7% in the brain, 1% in the cartilage, 10 to 13% in the liver, and 4 to 6% in the kidney, among others (22–26). This fact should be considered as well when creating the normoxic microenvironments for multiorgan-on-chips systems. In addition, oxygen regulates drug metabolism acting on tissues/organs due to lipid peroxidative reactions and reactive oxygen species attacking on enzymes and nucleic acids. It has been reported that hypoxia is essential since metabolic activation results in enhanced free radicals and oxygen involvement in lipid peroxidation (27). Thus, oxygen control should be considered in drug toxicity on microtissues in vitro too.

To ensure a physiological oxygen level in an organ-on-a-chip platform, a conventional approach is static culture in an incubator at a preset oxygen level (28, 29). Although the approach enables required oxygen levels for single-organ-on-a-chip cultures, the lack of automated, on-demand control within the culture medium might be the key limitation to maintaining constant normoxic levels of desire and the growth of different organs or tissues within the same culture (30), and hence cannot be used when multiple organ types on the chips are channels together in a single loop, beyond the fact that this method is difficult for oxygen monitoring in a real-time manner. The recently emerged on-chip oxygen-scavenging technologies have become attractive. For example, oxygen can be rapidly scavenged by an irreversible chemical reaction in the flowing microchannels through a polydimethylsiloxane (PDMS) membrane (31). Photocatalytic reactions could also be integrated with microfluidic devices to consume dissolved oxygen, while water electrolysis could generate oxygen across PDMS membranes (32). However, it has been rarely reported to incorporate oxygen scavengers with oxygen generator to allow precise control of local oxygenation in a self-sustaining manner. Moreover, most of the current oxygen-scavenging and -generating devices are used for cell culture in the half-open or open format without circulatory flows to mimic microenvironments in vivo. Commonly used organ-on-a-chip platforms are based on a PDMS material that also increases the difficulty to block exterior oxygen diffusion (33). In addition, the nonclosed microsystem may easily cause contamination. Therefore, it is necessary to develop an oxygen-controlling (multi)organ-on-chip(s) platform in a closed microcirculation system for recapitulating organ physiology and relevant drug studies.

Here, we report the development of an automated, closed-loop multiorgan-on-chips platform that provides dynamic, continuous, individually adjustable control and monitoring of oxygen levels in the flowing culture medium across different microtissue-on-chips in separation or in connection. This unique platform features four aspects: *i*) an automated oxygen-controlling and -monitoring system; *ii*) oxygen scavenger(s) for decreasing dissolved oxygen level(s) in a modular manner; *iii*) an oxygen generator for bringing the oxygen level to ambient; *iv*) and bioreactor(s) to host the desired microtissue(s). To create this modular oxygen-controlled microtissue-on-chips platform, all of the microfluidic chips were made from laser-patterned poly(methyl methacrylate) (PMMA) sheets and sealed by thermal treatment. The thermoplastic chips with a low oxygen-diffusion coefficient (2.7×10^{-8} cm^2 s^{-1}) would avoid gas exchange with external environments, unless when needed for oxygen scavenging or generation achieved with thin PDMS membranes. The platform was programmed by a computer and operated in an automated manner for at least 7 d evaluated. The geometry and performance of each microfluidic chip component were investigated separately, including the mini-microscope-based optical oxygen sensor(s), the oxygen scavenger(s), the mixer(s), the oxygen generator, and the bioreactor(s). The automated control system was further tested and analyzed. The control over the oxygen level in the platform was achieved in real time with continuous monitoring and dynamically adjusted to adapt to the need in the desired module. Independent longer-term assessments of drug responses and shorter-term evaluations of acute toxicities under different oxygen levels to the parallelly channeled liver, kidney, and arterial vessel microtissues were conducted without factoring in organ–organ interactions.

Results

The standard multiorgan-on-chips platforms are usually hosted in incubators that are supplied with the oxygen level at 21%, which is essentially hyperoxic to all tissue types. Fig. 1 shows the physiological ranges of oxygen levels in different human organs (Fig. 1*A*) (25). As such, utilization of fresh culture medium with 21% of oxygen level in vitro does not accurately represent the metabolic activities of tissues in the human body. Thus, it is an unmet need to modulate physiological oxygen levels in microenvironments of each microtissue in the (multi)microtissue-on-a-chip platform. The commonly used organ-on-a-chip platforms are made of oxygen-permeable PDMS (the oxygen permeability of PDMS is 800×10^{-10} cm^3(STP) cm^{-2} s^{-1} $cmHg^{-1}$) that is difficult to control oxygen levels (34). In this work, the entire microfluidic chips were made from laser-machined PMMA layers bonded together (Fig. 1 *B* and *C*), since PMMA is impermeable to dissolved oxygen [the oxygen permeability of PMMA is 0.155×10^{-10} cm^3(STP) cm^{-2} s^{-1} $cmHg^{-1}$ (35)]. Each chip was separately patterned via direct laser ablation. To allow the patterns with high precisions and defined geometries, the laser power and speed were optimized for the CO_2 laser beam (*SI Appendix*, Fig. S1 *A–D*). After surface smoothing and thermal treatment (*SI Appendix*, Fig. S1 *E* and *F*) (36), the thermoplastic microfluidic chips were assembled and integrated into a closed-loop circuit. To ensure sufficient oxygen and nutrient supplies at the vicinity of microtissues, the on-chip circulation was driven by a peristaltic pump primed at a flow rate of 200 μL h^{-1} powered by programmed MATLAB codes (37). These codes were also written to drive the optical sensor(s) that monitor oxygen level(s) in the system at predetermined time points and to control the pump(s) integrated with the oxygen scavenger(s). A flow rate monitor was also encoded into the program to monitor the flow rate as well as potential channel blockage or leakage.

The closed-loop organ-on-a-chip platform was designed to be modular, including a programmable controlling system for microfluidic routing, oxygen level regulation, and real-time monitoring, bioreactor(s) for housing the microtissue(s), customized mini-microscope(s) integrated with optical oxygen sensor(s), oxygen scavenger(s) connected to flow rate-controlling pumps, and an oxygen generator for global oxygen exchange (Fig. 1*B*). To mimic the physiological microenvironments in the human body, the entire closed-loop platform was installed in a customized benchtop incubator maintained at 37 °C, 5% ambient CO_2, and 21% ambient oxygen that was connected to an oxygen-controlling and -monitoring system (Fig. 1 *B*, *i*). The classificator code allowed the system to automatically alter the flow rate on each chip until the desired oxygen level was reached, based on the optical sensor(s)' monitoring. Alternatively, a custom-made user interface enabled direct control over the pumps and a real-time

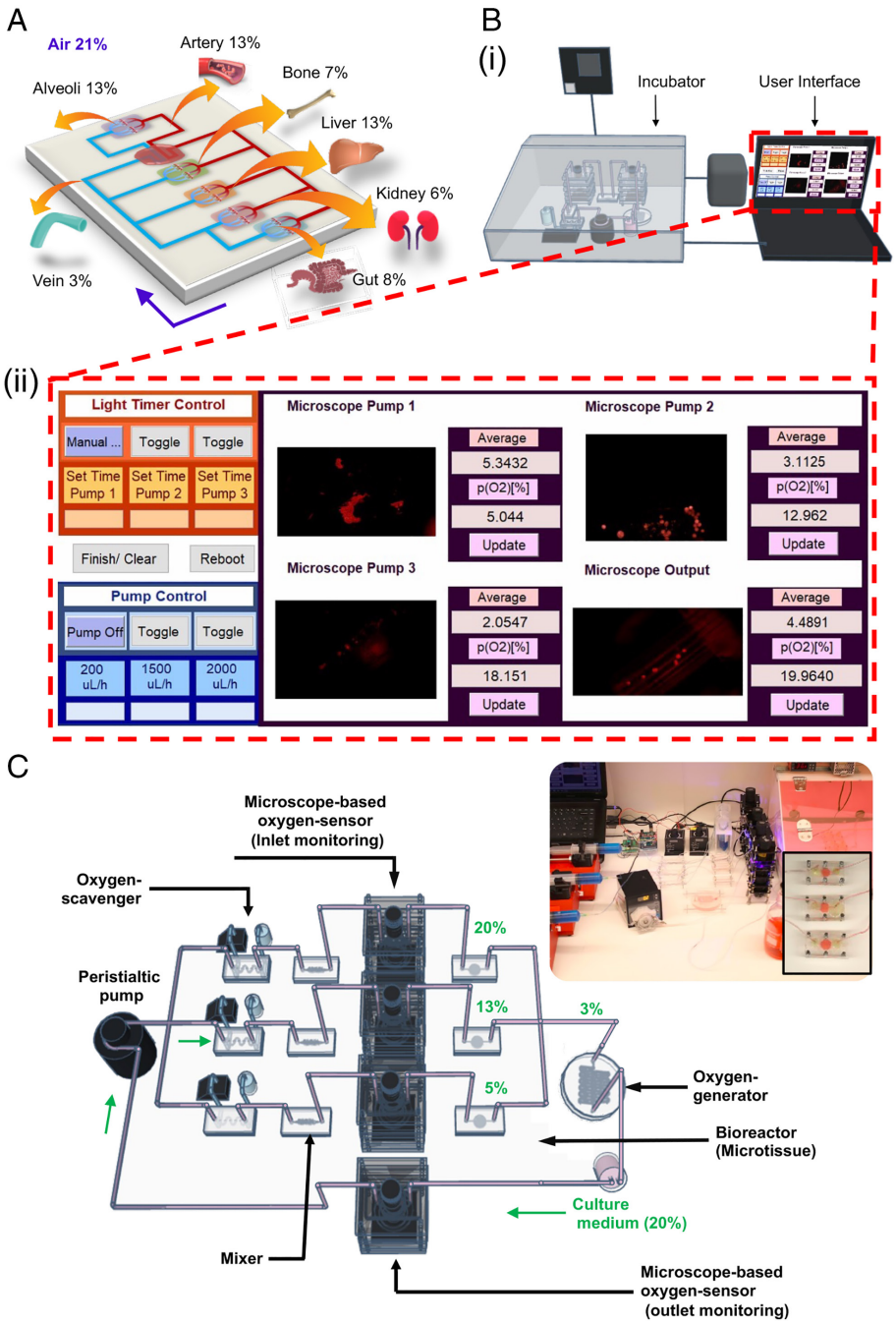

Fig. 1. An automated, closed-loop oxygen-controlled multiorgan-on-chips platform. (*A*) Physiological oxygen levels in various human organs. (*B*) (*i*) Schematic design of the entire platform embedded with programmed automation controls and a monitoring system. (*ii*) Screenshots of the user interface of the controller in real-time oxygen monitoring, featuring "a. Light Timer Control (working times for mini-microscopes)," "b. Pump Control (flow rates for oxygen scavengers 1, 2, and 3)," and "c. Monitoring Window (real-time monitoring fluorescent oxygen sensor changes from the mini-microscope-based optical oxygen sensors connected to the oxygen scavenger pumps)". (*C*) Schematic design of a representative platform, which mainly contains four customized mini-microscope-based optical oxygen sensors to monitor oxygen levels of the inlet and the outlet of each bioreactor (microtissue), oxygen scavengers (consisting of oxygen-scavenging chips connected with syringe pumps for the bottom layers, and a peristaltic pump for the top layers), an oxygen generator, and a peristaltic pump for driving the circulation. The *Inset* shows the photograph of the actual fabricated platform.

visualization of the oxygen sensors. Individual modules were interconnected by using Teflon tubes, which allowed for fluid flow in the circulation. The oxygen level in each microchannel was controlled by "Light Timer Control" (excitation duration of the mini-microscopes), "Pump Control" (syringe pumps connected to the oxygen scavengers), and real time monitored in "Microscope Pump" (Fig. 1 *B*, *ii*). "Microscope Output" was designed to monitor the oxygen level in the recycled culture medium. To ensure that the platform is compatible with multiple tissues that require different oxygen levels, several branches of the microfluidic channels could be designed to maintain intended oxygen levels (e.g., 5%, 13%, and 20%, respectively) in the desired microtissue modules (Fig. 1*C*). As the microtissues normally consume the dissolved oxygen in the culture medium, the oxygen level at the outlet of the microtissues was preset to 3% and monitored in "Microscope Output."

Real-Time Oxygen-Monitoring and -Controlling Systems. To achieve real-time monitoring of oxygen levels within the system, a customized microfluidic oxygen sensor was integrated, where the fluorescence emission intensity of the sensing microbeads was observed and converted to the dissolved oxygen level in the programmed software (25, 33). The fluorescent oxygen-sensing beads were produced by using a flow-focusing microfluidic droplet generator, which could encapsulate oxygen-sensitive fluorescent dye [tris(4,7-diphenyl-1,10-phenanthroline)ruthenium(II) dichloride] in a PDMS matrix (33, 34). These as-synthesized oxygen-sensing microbeads were well dispersed, where the average diameter was approximately 20 μm (*SI Appendix*, Fig. S2). To ensure the real-time monitoring of the oxygen level of the flowing culture medium in the microchannel, the fluorescent microbeads were fixed on the surface of the microchannel. The microfluidic oxygen-sensing chip was installed in a customized mini-microscope (33), where the emission

of the sensing microbeads could be observed under the excitation of a high-intensity 470-nm light-emitting diode (LED) (Fig. 2 *A* and *B*) and directly monitored by a color complementary metal–oxide–semiconductor (CMOS) chip. The CMOS chip integrated with the custom-coded program could then split a captured image into the red (R), green (G), and blue (B) channels and analyze the emission intensities. As expected, a high emission intensity signal was observed in the R channel of the captured image, while the signals of G and B channels were negligible (Fig. 2*C*).

Stability is an important parameter for long-term oxygen monitoring by using the fluorescent oxygen sensor. One approach is to decrease the decay time of the fluorophores. The intrinsic fluorescence decay as the exposure time was prolonged, was assessed. The ΔI of the oxygen sensor decay decreased as the exposure time was prolonged to 180 min. The fluorescence decay was stable after 150 min. The fluorescence decay is described by the Stern–Volmer equation:

$$\frac{\tau_0}{\tau_n} = 1 + K_q\left[O_2\right]_n, \qquad [1]$$

where τ_0 represents sensor lifetime at 0% of the oxygen level, τ_n is the sensor lifetime at the measured oxygen level $\left[O_2\right]_n$, and K_q is the Stern–Volmer quenching constant (2.7×10^{-3} μmol L^{-1}). Following the 180-min light exposure, the response time and reversibility of the oxygen sensor were evaluated. The result in Fig. 2*D* shows that as the oxygen level was decreased from 20 to 5%, the measured response time was 140 s and the emission intensity increased 1.2-fold. When the oxygen level was increased from 5 to 20%, the response time was 60 s and the emission intensity decreased by 1.2-fold. After six cycles, the emission intensity could be maintained at the original level, demonstrating high stability and reversibility of the microfluidic oxygen sensor. The standard curve of the oxygen sensor is shown in Fig. 2*E*. The effective detection range of the oxygen sensor was between 20% and 0%, where the emission intensity increased linearly. The sensitivity of the sensor was calculated to be $0.02\%^{-1}$. Therefore, the developed microfluidic oxygen sensor could be used for real-time monitoring of oxygen levels in the microfluidic chip within the physiological range.

Dynamic Oxygen-Scavenging and Mixing Systems. To rapidly deplete excessive oxygen from the culture medium, an oxygen scavenger was designed to integrate with the organ-on-a-chip platform. Sodium sulfite (Na_2SO_3) is a promising reagent that can irreversibly consume dissolved oxygen in the solution, producing harmless sodium sulfate (Na_2SO_4) (38). To accelerate the rate of reaction, cobalt sulfate ($CoSO_4$) was added as a catalyst following the reactions specified below (39):

$$\begin{aligned} &6CoSO_4 + 2H_2O + O_2 \rightarrow 2Co_2(SO_4)_3 + 2Co(OH)_2 \\ &Co_2(SO_4)_3 + Co(OH)_2 + Na_2SO_3 \rightarrow Na_2SO_4 \\ &+ 3CoSO_4 + H_2O. \end{aligned} \qquad [2]$$

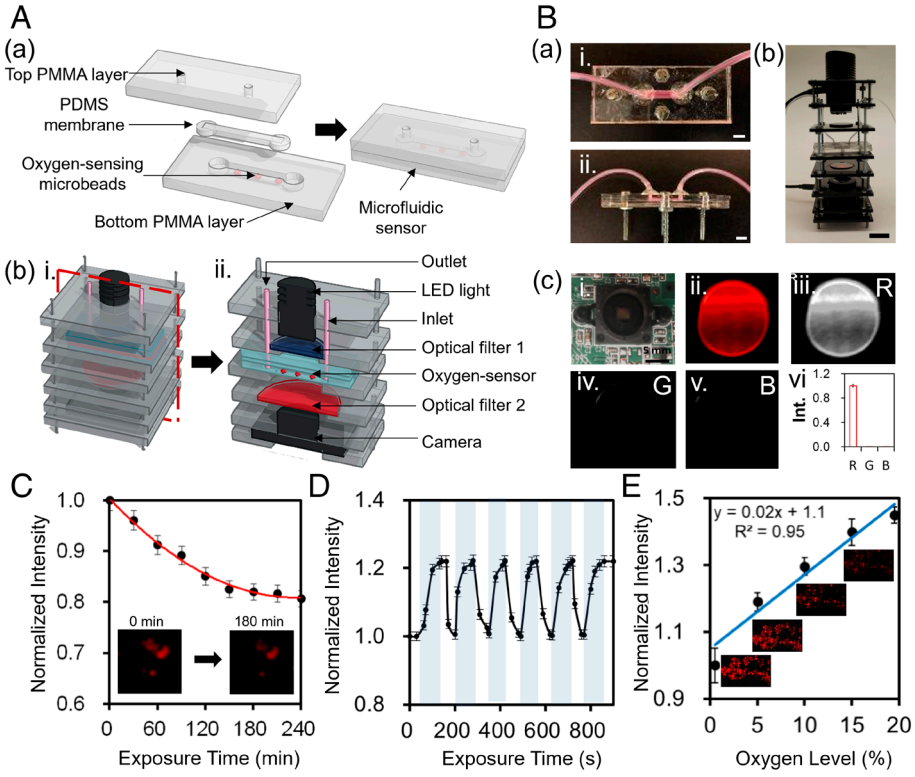

Fig. 2. Customized microfluidic optical setups for real-time oxygen monitoring. (*A*) Schematic of the mini-microscope-based optical setup, including a multilayered microfluidic thermoplastic chip embedded with fluorescent oxygen-responsive microbeads and a fluorescence microscope module. (*a*) The microfluidic chip consisted of a top PMMA layer engraved with a straight microchannel, a bottom layer deposited with fluorescent microbeads, and a PDMS membrane directly cured on the bottom surface holding the microbeads in place. The inlet and outlet of the chip were connected with tubing for fluid flow. (*b*) (*i*) The mounted mini-microscope contained (*ii*) a high-intensity blue LED as the light source, optical filters for excitation and emission, and a camera assembled at the bottom of the microscope. (*B*) Photographs of the optical oxygen-sensing setup. (*a*) (*i*) *Top* view and (*ii*) side view of the microfluidic oxygen sensor. (Scale bar, 5 mm.) (*b*) Mounted mini-microscope. (Scale bar, 3 cm.) (*c*) Camera for fluorescence imaging. (*i*) The CMOS sensor disassembled from the webcam. (*ii*–*v*) RGB and R/G/B images of the fluorescent oxygen probe showing the separation of R, G, and B colors by the encoded MATLAB program. (*vi*) Quantification measurement of fluorescence intensity showing the accuracy and sensitivity of the digital channel-separation approach. (*C*) Fluorescence quenching curve of the oxygen sensor using the mini-microscope. The *Inset* shows the captured fluorescence images before and after photobleaching for 4 h (n = 3). (*D*) Stability of the measurement using the fabricated oxygen sensor setups for 6 cycles (n = 3). (*E*) Calibration curve of the optical oxygen sensor. *Insets* show the captured fluorescence images at different oxygen concentrations (n = 3).

However, the direct addition of Na_2SO_3 and $CoSO_4$ to the circulating medium is unrealistic to microtissue culture due to the toxicity of the scavenging solution and the unnecessary need for alteration of the shear force acting on the microtissues when changing the oxygen levels based on scavenging solution flow rate. Thus, a thermoplastic microfluidic chip was fabricated with three layers, where a PDMS membrane with a thickness of 20 μm was sandwiched between the engraved PMMA layers to seal the open microchannels and separate the two flow layers (Fig. 3*A*). The culture medium flows within the microchannel of the top layer in the scavenger (Fig. 3 *B*, *i* and *ii*), while the mixture of Na_2SO_3 and $CoSO_4$ flows within the bottom microchannel. Since PDMS has high selectivity to oxygen and poor permeability to the aqueous solution and the chemical species, dissolved oxygen molecules in the culture medium could diffuse into the scavenging solution through the PDMS membrane and rapidly diminished there. The optimization of the PDMS membrane in terms of the ratio of polymer base and curing agent was investigated to achieve the highest oxygen permeability. PDMS membranes with different ratios at 8:1, 10:1, and 12:1 were utilized to fabricate oxygen scavengers (*SI Appendix*, Fig. S3). The oxygen-depletion effect of the scavengers was assessed by real-time measurements of the oxygen levels at the outlet of the main channel in each oxygen scavenger while the inlet of the scavenger was supplied with fresh culture medium (20 to 21% of oxygen). It was observed that the oxygen-depletion effect increased 51.2% as the ratio was elevated from 8:1 to 12:1. As the flow rate was ramped up from 1,000 to 2,000 μL h^{-1}, the oxygen-depletion effect increased from 26.7 to 38.7% at different ratios. The result demonstrated that the oxygen permeability of PDMS membrane was improved as the ratio was increased since the higher ratio resulting in a less concentrated polymer network would allow for oxygen diffusion more easily. However, when the ratio was higher than 13:1, the PDMS membrane was too soft to use. Therefore, the ratio of polymer base and curing agent at 12:1 was applied for the following experiments.

To generate homogenous oxygen levels in the flowing culture medium, a chaotic mixer was designed and connected with the outlet of the scavenger (*SI Appendix*, Fig. S4). The mixer with patterns of grooves fabricated by direct laser writing could generate transverse flow in the microchannel, making it possible to apply efficient microscale flow mixing (Fig. 3*C*) (40). The manipulation of oxygen levels in the culture medium was investigated by adjusting the flow rate and scavenging reagent concentration in the bottom microchannel of the scavenger. The oxygen level of the culture medium downstream was monitored by the above-mentioned oxygen sensor. As the flow rate was increased from 1,000 to 2,000 μL h^{-1}, the oxygen level decreased linearly. The highest value of oxygen depletion was 63.0% when the Na_2SO_3 concentration was 20 wt%. As the Na_2SO_3 concentration was decreased to 2 wt%, the oxygen depletion dropped to 24.3%. To ensure that the oxygen scavenger could supply the culture medium with a wide range of oxygen levels, Na_2SO_3 at the concentration of 20 wt% was chosen for the subsequent studies. $CoSO_4$ at a concentration of 0.02 wt% was used as the catalyst to accelerate oxygen depletion by the scavenging agent. Thus, the oxygen level in the outlet was designed to be controlled by adjusting the flow rate of the scavenger. The result showed that the oxygen level was approximately 13% when the flow rate was set to 1,000 to 1,250 μL h^{-1}. To obtain the oxygen level at 5%, the flow rate was set to 1,750 to 2,000 μL h^{-1}. The stability of the system was estimated by monitoring the oxygen level every 30 min. After a 3-h observation, the oxygen level was maintained compared to the initial measurement (Fig. 3 *D*, *Inset*). Cropped micrographs from the user interface further evidenced that as the flow rate was increased from 1,000 to 2,000 μL h^{-1}, the emission intensity increased (Fig. 3*E*).

Dynamic Oxygen-Generating System. A closed-loop modular organ-on-a-chip platform requires the culture medium to be ideally circulated in the entire system. Since oxygen is constantly consumed by microtissues in the platform, the increase in oxygen level from a low level to 20 to 21% should be considered, and in fact, is essential. Accordingly, an oxygen generator was designed that was composed of a microfluidic chip sealed with a PDMS membrane with a thickness of 50 μm (Fig. 4*A*). Again, since the PDMS membrane has a high permeability to oxygen molecules at 35 to 37 °C (800×10^{-10} cm^3(STP) cm^{-2} s^{-1} $cmHg^{-1}$), the dissolved oxygen level could be effectively increased by exchanging with oxygen in the ambient air, functioning as an artificial breathing "lung" that oxygenates the "blood" (medium). For well mixing the flowing culture medium in the oxygen generator, staggered herringbone patterns were fabricated at the bottom of the microchannel, where the culture medium could perfuse without any noticeable leakage (Fig. 4*B*). The oxygen levels at the inlet and the outlet of the oxygen generator were measured to be <4% and

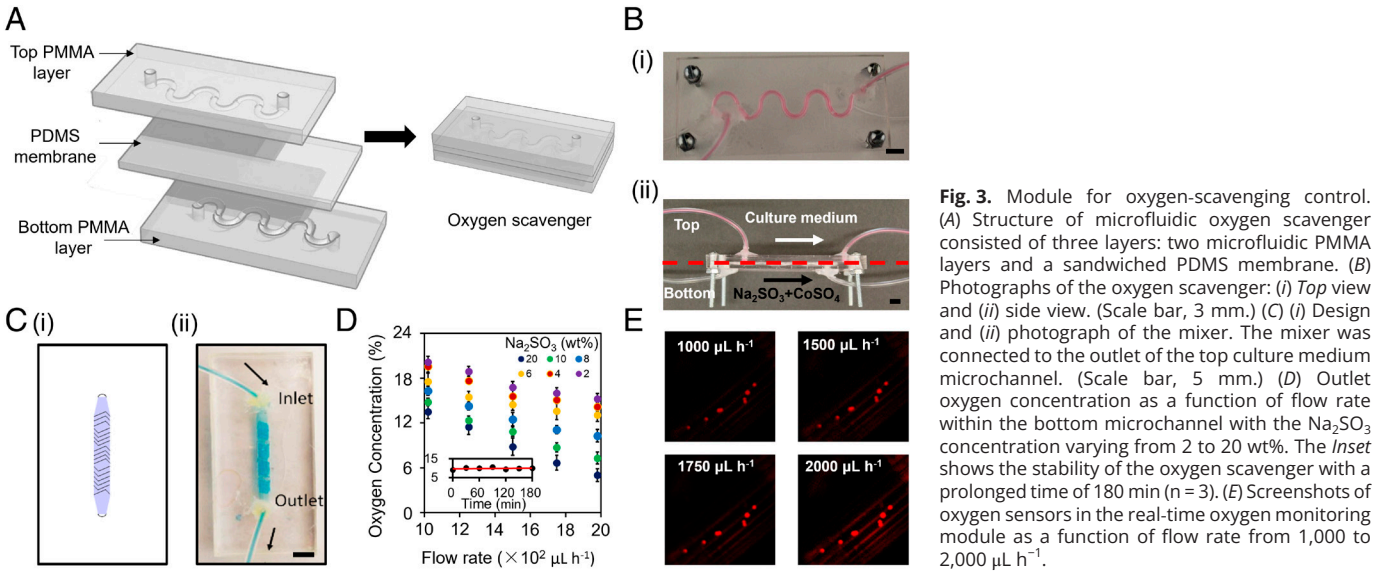

Fig. 3. Module for oxygen-scavenging control. (*A*) Structure of microfluidic oxygen scavenger consisted of three layers: two microfluidic PMMA layers and a sandwiched PDMS membrane. (*B*) Photographs of the oxygen scavenger: (*i*) *Top* view and (*ii*) side view. (Scale bar, 3 mm.) (*C*) (*i*) Design and (*ii*) photograph of the mixer. The mixer was connected to the outlet of the top culture medium microchannel. (Scale bar, 5 mm.) (*D*) Outlet oxygen concentration as a function of flow rate within the bottom microchannel with the Na_2SO_3 concentration varying from 2 to 20 wt%. The *Inset* shows the stability of the oxygen scavenger with a prolonged time of 180 min (n = 3). (*E*) Screenshots of oxygen sensors in the real-time oxygen monitoring module as a function of flow rate from 1,000 to 2,000 μL h^{-1}.

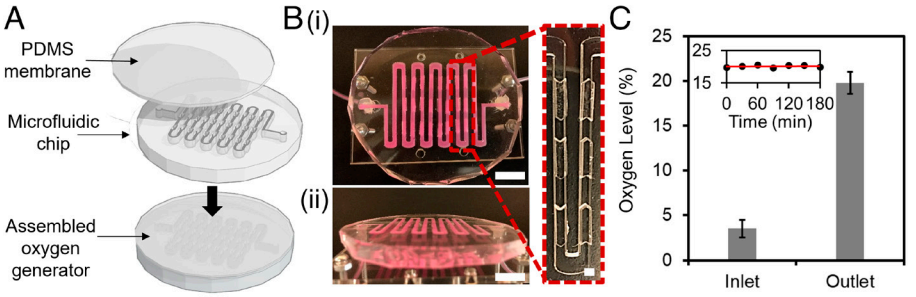

Fig. 4. Module for oxygen generation. (*A*) Schematic design of the oxygen generator. The bottom layer was patterned with microchannel, while the PDMS membrane was bonded on top to seal the microchannel. (*B*) Photographs of the oxygen generator in (*i*) *Top* view and (*ii*) side view. Food dye within the microchannel was used to demonstrate fluid flow. The magnified image shows the staggered herringbone patterns in the microfluidic channel to aid mixing. (Scale bar, 1.5 cm.) *Inset* scale bar, 2 mm. (*C*) Measured oxygen levels at both inlet and outlet. The *Inset* shows the stability of the oxygen generator with a prolonged test time of 180 min (n = 3).

20%, respectively (Fig. 4*C*). Longer-term monitoring of oxygen levels at the outlet shows that as the time was prolonged to 3 h, the measured oxygen level was still maintained at approximately 20% (Fig. 4 *C*, *Inset*), which demonstrated the high stability of the oxygen generator.

The geometry of the bioreactor was adopted from our previous reports to ensure a uniform fluid flow distribution (Fig. 5*A*) (37). A configuration featuring an array of 45 cell-encapsulating 3D microstructured gelatin methacryloyl (GelMA) dots was designed to emulate the microtissue as a proof of concept (Fig. 5*B*) (37). The cell-encapsulated GelMA hydrogel was micropatterned to allow for culture medium flow and oxygen exchange. The oxygen level at the inlet was kept constant at 13%. To ensure the oxygen level at the outlet to remain at 3%, which is comparable to the oxygen level in the venous blood in general scenarios, cell number and flow rate were optimized in the simulation. As the cell number was increased from 0.4×10^6 to 1.0×10^6 cell mL^{-1} (the flow rate was set to 200 $\mu L\ h^{-1}$) and the flow rate was decreased from 800 to 200 $\mu L\ h^{-1}$ (the cell density was set to 1×10^6 cell mL^{-1}), the numerically simulated oxygen level decreased from 8 to 3% (Fig. 5*C*).

The fabricated thermoplastic bioreactor shown in Fig. 5*D* contained a microtissue, which was fabricated by photopatterning. To guarantee sufficient oxygen diffusion and culture medium flowing within the microtissue, 3D GelMA-encapsulated cells were patterned into a dot array as the microtissue at the bottom of the bioreactor. The bioreactor was assembled with resealability that allowed for convenient postanalyses of the microtissue (Fig. 5*D*) (37). Higher flow rates of the culture medium would increase laminar shear force exerted across the microtissue, while lower flow rates could not provide sufficient oxygen diffusion within the microtissue. Therefore, 200 $\mu L\ h^{-1}$ and 1×10^6 cell mL^{-1} were applied throughout the subsequent experiments.

Effects of Oxygen Levels on Biological Behaviors and Drug Responses. To investigate the oxygen effects on physiological and metabolic activities of our multiorgan-on-chips platform, a static 3D microtissue culture as a conventional method was first developed. The liver is the main organ for drug metabolism, and the hepatic artery is the major source of oxygen for the hepatic cells (41). The oxygen availability would be expected to differ at different parts of the liver, according to the supply of blood, where the most common range is 10 to 13% and can be lowered in certain other areas (42). The 3D liver microtissues were fabricated by applying the photolithography technique to GelMA hydrogel-encapsulated human hepatic spheroids. A static culture placed the 3D liver microtissues in the hypoxia incubator setting the oxygen levels to 5%, 13%, or 20%, separately (*SI Appendix*, Fig. S5*A*), and supplemented with fresh standard culture medium every 2 d. The immortal human hepatocellular carcinoma (HepG2/C3A) cells have been shown to exhibit the main functions of liver tissues (43). Accordingly, the 3D GelMA-encapsulated HepG2/C3A cells were used to create liver microtissues. The viability of the liver microtissues was evaluated by a Live/Dead assay, in which the live cells were stained in green, while dead cells in red. It was shown that

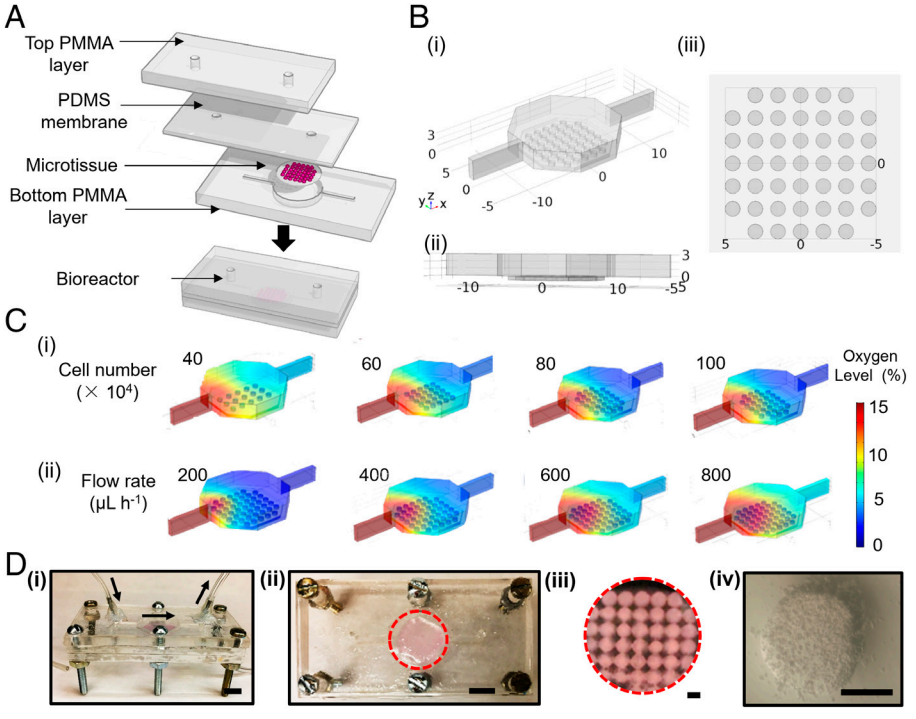

Fig. 5. Design of a proof-of-concept individual microtissue-on-a-chip platform. (*A*) Schematic of the microtissue-embedded bioreactor where the patterned cell-encapsulated 3D microgel array was embedded within the bottom PMMA layer and covered with a top PMMA layer. An elastic PDMS membrane was sandwiched between PMMA layers for sealing. (*B*) Schematics of the microtissue-embedded bioreactor: (*i*) geometry; (*ii*) side view; and (*iii*) microtissue design. (*C*) Simulation of oxygen consumption as a function of (*i*) cell density at the flow rate of 200 $\mu L\ h^{-1}$ and (*ii*) flow rate at the cell density of 1×10^6 cell mL^{-1} in the bioreactor. (*D*) Photographs of the bioreactor (microtissues): (*i*) side view and (*ii*) *top* view, (Scale bar, 5 mm). (*iii*) Microtissues (Scale bar, 1 mm), and (*iv*) a single 3D micro-GelMA dot (3D encapsulated cells) (Scale bar, 0.5 mm).

the viabilities of the liver microtissues at the oxygen level of 13% were 31% and 23% higher than the counterparts at the oxygen levels at 5% and 20% on Day 7, respectively (*SI Appendix*, Fig. S5 *B*, *i* and *ii*). Proliferation evaluations using the PrestoBlue assay further validated that the liver microtissues were more amenable to survival at the oxygen level of 13% (*SI Appendix*, Fig. S5 *B*, *iii*). Albumin is synthesized in the liver, where its functions include maintaining osmotic pressure and transporting a variety of circulating molecules (44). Serum albumin levels are manipulated via hepatic tissue secretion, mass exchange among the intra- and extravascular compartments, protein levels, lymphatic uptake, and body changes (45). The functions of the liver microtissues were investigated by the assessments of albumin production. After a 7-d incubation, albumin production of the liver microtissue at the oxygen level of 13% was 2.1-fold and 0.8-fold higher than the counterparts at the oxygen levels of 5% and 20%, respectively (*SI Appendix*, Fig. S5 *B*, *iv*). These results demonstrated that the liver microtissues exhibited favorable activities at the oxygen level of 13%, which was consistent with previous studies (25, 26), while 5% was hypoxic and 20% was hyperoxic to the liver microtissues.

The kidney is the main organ to eliminate drugs from the body (46). To mimic the kidney, the similar fabrication process was also applied to produce nephric microtissues by 3D encapsulation of nephric spheroids. HK-2 cells, immortalized proximal tubule epithelial cells from the normal adult human kidney (47), were used to produce nephric spheroids and encapsulated within the 3D micro-GelMA dots. The viabilities and proliferation activities of the statically cultured kidney microtissues in the hypoxia incubator confirmed that the oxygen level at 5% was the most functional for kidney microtissues as compared with the higher oxygen levels at 13% and 20% (*SI Appendix*, Fig. S6 *A* and *B*, *i–iii*). Kidney injury molecule-1 (KIM-1) is a biomarker that can be up-regulated in acutely and chronically injured kidney tissues (48). The functions of the kidney microtissues were investigated by the detection of the secreted KIM-1 levels. The KIM-1-expression of the kidney microtissues at 5% of the oxygen level was 76% and 93% lower than the counterparts at 13% and 20% of the oxygen levels after a 7-d incubation, respectively (*SI Appendix*, Fig. S6 *B*, *iv*). Thus, the oxygen level of 5% was deemed the most suitable for static culture of kidney microtissues in the conventional hypoxia incubator.

The blood vessel is an organ that transports blood throughout the body by the circulatory system (49). To mimic the blood vessel, the same photolithography technique was utilized to produce GelMA hydrogel-encapsulated human umbilical vein endothelial cells (HUVECs), which is a typical model cell for studying arterial blood vessels. The vessel microtissues exhibited the optimal behaviors at the oxygen level of 13% in the viability and proliferation activity tests as compared to the oxygen levels at 5% and 20% (Fig. 6 *B*, *i–iii* and *SI Appendix*, Fig. S7*A*). Endothelin 1 (ET-1) is a potent endogenous vasoconstrictor that is secreted from dysfunctional endothelial cells (50). As compared to the secretion of ET-1 in the vessel microtissues at the oxygen levels of 5% and 20%, the ET-1 level in the vessel microtissues at the oxygen level of 13% was the lowest throughout the 7-d incubation (*SI Appendix*, Fig. S7, *iv*). The results demonstrated that the oxygen level at 13% was suitable for the static culture of the 3D arterial vessel microtissue in the hypoxia incubator. Taken all together, the liver, kidney, and arterial vessel microtissues are sensitive to both hypoxia and hyperoxia. Lower oxygen levels are more likely insufficient to provide enough oxygen to mitochondria for aerobic metabolism of microtissues, while higher oxygen levels would accelerate the progression of pathological phenotypes (51).

To reconfirm the optimal oxygen level of each microtissue-on-a-chip model, the 3D liver, kidney, and arterial vessel microtissues were separately placed in their bioreactors and integrated to the oxygen-controlling systems to form three individual organ-on-a-chip platforms, where the culture medium was driven by syringe pumps. By adjusting the parameters of the oxygen scavengers, the oxygen levels in the flowing culture media were controlled at 5%, 13%, and 20%, respectively, optimized levels for the respective organ types (*SI Appendix*, Figs. S8–S10). The viability test of the individual liver-on-a-chip showed that the viability at 13% of the oxygen level was 22% and 12% higher than those at 5% and 20% of the oxygen levels, respectively (*SI Appendix*, Fig. S8 *B*, *i* and *ii*). The proliferation test further demonstrated that the liver microtissue-on-a-chip at 13% of the oxygen level showed 47% and 17% higher proliferation than the counterparts at 5% and 20% of the oxygen levels, respectively, after the 7-d incubation (*SI Appendix*, Fig. S8 *B*, *iii*). Moreover, the liver microtissue-on-a-chip produced 40% and 18% higher of albumin at the oxygen level of 13% than the counterparts at 5% and 20%, respectively (*SI Appendix*, Fig. S8 *B*, *iv*). Compared to the conventional static culture, the individual liver-on-a-chip integrated with the built-in oxygen-controlling systems showed similar results that the oxygen level at 13% in the culture medium was the most beneficial for the liver microtissue. Similar assembling processes of bioreactors, oxygen scavengers, and oxygen sensors were also applied to individual kidney microtissue-on-a-chip (*SI Appendix*, Fig. S9*A*) and individual arterial vessel microtissue-on-a-chip (*SI Appendix*, Fig. S10*A*) cultures. The viabilities, proliferation, and metabolic activities of the kidney microtissue-on-a-chip and vessel microtissue-on-a-chip proved that the optimal oxygen level for the kidney microtissue was 5% and for the vessel microtissue was 13% (*SI Appendix*, Figs. S9 and S10), which again, were consistent with the static culture studies (*SI Appendix*, Figs. S6 and S7).

All the modules were subsequently integrated to form a closed-loop modular multiorgan-on-chips platform, where the culture medium was circulated and driven by a peristaltic pump (*SI Appendix*, Fig. S11). Each branch of the microtissue (liver, kidney, and arterial vessel)-on-a-chip connected to an oxygen scavenger and a real-time-monitoring oxygen sensor, together with a global oxygen generator, all embedded with programmed automation controls, was assembled in parallel. The automation system was controlled in the user interface. Whether the developed closed-loop modular multiorgan-on-chips platform could independently control the dissolved oxygen in the flowing culture medium at the optimal level for each connected microtissue-on-a-chip was investigated (Fig. 6). To this end, based on the optimal oxygen level for each microtissue (*SI Appendix*, Figs. S5–S10), the oxygen levels were independently controlled and monitored at 13% in both the connected liver microtissue-on-a-chip and the connected arterial vessel microtissue-on-a-chip, and at 5% in the connected kidney microtissue-on-a-chip (Fig. 6 *A*, *i*). The viabilities as well as proliferation and metabolic activities of the connected liver, kidney, and arterial vessel microtissue-on-chips at their respective optimal oxygen levels were studied (Fig. 6 *A*, *ii–iv*).

For the connected liver microtissue-on-a-chip at the optimal oxygen level of 13%, the viability was calculated to be 94% after the 7-d incubation where no significant differences were observed from the hypoxia incubator-based (95%) and individual microtissue-on-a-chip-based (92%) cultures (Fig. 6 *A*, *ii* and *iii* and *SI Appendix*, Figs. S5 B, *i* and *ii* and S8 *B*, *i* and *ii*). In addition, the viability test of the liver microtissue in Fig. 6 *A*, *ii* and *iii* showed that dead cells (stained in red) were mainly distributed in the center of each dot (Ø: 0.8 mm, h: 0.5 mm). As the flow rate of the culture medium was maintained at 200 μL h^{-1}, this observation was possibly due to distribution differences of oxygen and nutrient concentrations within the hydrogel matrix caused

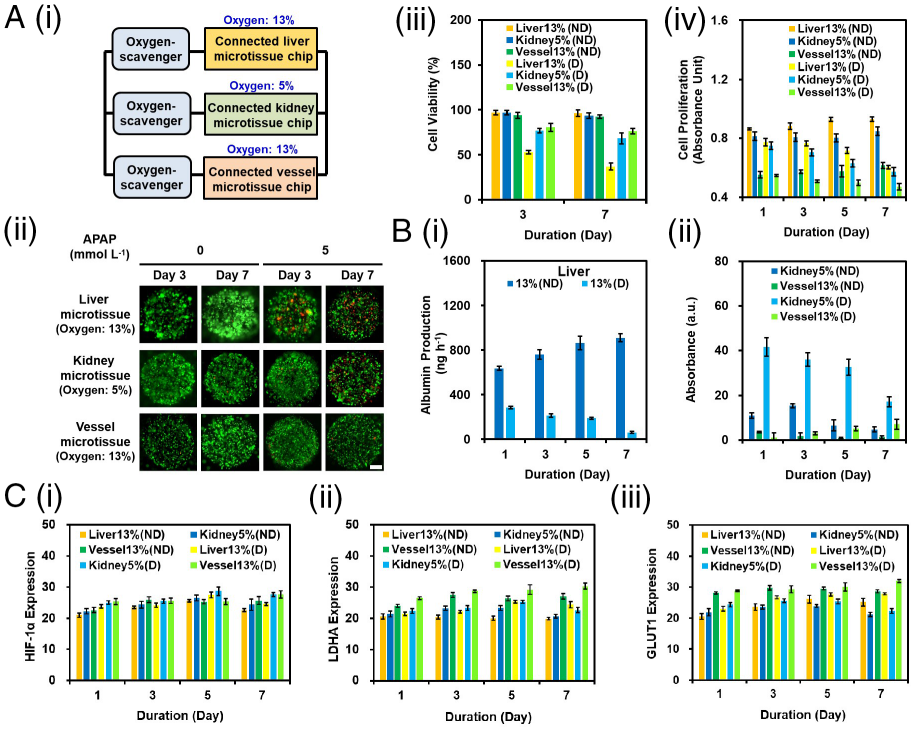

Fig. 6. Evaluations of oxygen effects on physiological activities and toxicity of APAP poisoning in our closed-loop multiorgan-on-chips platform. (*A*)(*i*) Schematic of the experimental design at different optimal oxygen levels. Live/dead assays [(*ii*) fluorescence micrographs and (*iii*) quantitative analyses] of 3D micro-GelMA dots (scale bar, 200 μm), (*iv*) proliferation activities, and (*B*) metabolic activities [(*i*) albumin productions and (*ii*) KIM-1 and ET-1 secretions] of the multiorgan-on-chips platform in the presence of APAP poisoning (5 mmol L^{-1}) at different optimal oxygen levels: liver at 13%, kidney at 5%, and vessel at 13%. (*C*) (*i*) HIF-1*α*, (*ii*) LDHA, and (*iii*) GLUT1 expressions of the multiorgan-on-chips platform upon in the presence of APAP (5 mmol L^{-1}). "ND" indicates no drug (APAP), while "D" represents drug (n = 3).

by the diffusion effect, which is also a good mimicry of native tissues since the liver tissues show zonation (52). Similarly, the proliferation activities and albumin production of the connected liver microtissue-on-a-chip was 0.93 and 911 ng h^{-1}, which was consistent with 0.88 and 890 ng h^{-1} of the conventional static culture after the 7-d incubation (Fig. 6 *A*, *iv* and 6 *B*, *i* and *SI Appendix*, Fig. S5 *B*, *iii* and *iv*).

For the connected kidney microtissue-on-a-chip at the optimal oxygen level of 5%, the viabilities were calculated to be 97% and 96% on Days 3 and 7, which were similar to 96% and 89% of the conventional static culture in the hypoxia incubator and 97% and 96% of the individual kidney microtissue-on-a-chip culture (Fig. 6 *A*, *ii* and *iii* and *SI Appendix*, Figs. S6 *B*, *i* and *ii* and S9 B, *i* and *ii*). The proliferation activities in the connected kidney microtissue-on-a-chip were 11% higher than the conventional static and the individual microtissue-on-a-chip cultures, respectively (Fig. 6 *A*, *iv* and *SI Appendix*, Figs. S6 *B*, *iii* and S9 *B*, *iii*). In addition, KIM-1 levels of the connected kidney microtissue-on-a-chip culture were 15% and 12% lower than the corresponding levels of the static culture in the hypoxia incubator and the individual kidney microtissue-on-a-chip culture (Fig. 6 *B*, *ii* and *SI Appendix*, Figs. S6 *B*, *iv* and S9 *B*, *iv*), which demonstrated that the connected kidney microtissue-on-a-chip had lower injury.

For the connected vessel microtissue-on-a-chip at the optimal oxygen level of 13%, the viability was 92%, which was similar to the viabilities of 98% in the hypoxia incubator and 95% in the individual vessel microtissue-on-a-chip (Fig. 6 *A*, *ii* and *iii* and *SI Appendix*, Figs. S7 *B*, *i* and *ii*, and S10 *B*, *i* and *ii*). The proliferation activity and the ET-1 level of the connected vessel microtissue-on-a-chip were also comparable to those of the static cultured vessel microtissue and the individual vessel microtissue-on-a-chip cultures (Fig. 6 *B*, *ii* and *SI Appendix*, Figs. S7 *B*, *iv* and S10 *B*, *iv*). Other oxygen levels were further applied to each connected microtissue-on-a-chip in the closed-loop multiorgan-on-chips platform, such as 5%, 13%, and 5% for liver, kidney, and arterial vessel microtissues, respectively (*SI Appendix*, Fig. S12). Conventional multiorgan-on-chips cultures were also used as a comparison by adopting the standard culture medium at the oxygen level of 20% (*SI Appendix*, Fig. S13). The viabilities as well as proliferation and metabolic activities of these two scenarios were both lower than the multiorgan-on-chips platform supplemented with oxygen at the optimal levels to the intended organ types. Altogether, the developed modular closed-loop multiorgan-on-chips platform could independently and tightly control the oxygen level in each connected microtissue-on-a-chip to continuously supply culture medium for each microtissue at its own optimal concentration.

Since the conventional approach to control oxygen levels of multiorgan-on-chips is to incubate them collectively in a hypoxia incubator that could only control the oxygen in the culture medium at a single level, the oxygen effects on all microtissue-on-chips in this configuration were further observed. The connected liver, kidney, and arterial vessel microtissue-on-chips system without oxygen-controlling units were placed altogether in the hypoxia incubator providing the oxygen level at 5%, 13%, or 20%, each at a time (Fig. 7 and *SI Appendix*, Fig. S16). It was shown that after the 7-d incubation, the viabilities of liver, kidney, and vessel microtissues at the unified oxygen level of 5% were 70%, 94%, and 80%, respectively, while those at 13% were 96%, 80%, and 98%, and those at 20% were 74%, 64%, and 85% (Fig. 7 *A*, *ii* and 7 *B*, *ii* and *SI Appendix*, Figs. S14–S16 *B*, *ii*). The liver and arterial vessel microtissues showed highest viabilities at the oxygen level of 13%, while the kidney microtissues showed a low viability at this oxygen level. Similarly, the proliferation activities of all the connected microtissue-on-chips in the hypoxia incubator at 13% of the oxygen level showed the highest levels in the liver microtissue and vessel microtissue (Fig. 7 *B*, *iii*) as compared with the counterparts at the oxygen level of 5% (Fig. 7 *A*, *iii*) and 20% (*SI Appendix*, Fig. S16 *B*, *iii*), whereas the proliferation activity was higher in kidney microtissue-on-a-chip at 5% (Fig. 7 *A*, *iii*) than those at the oxygen levels of 13% and 20% (Fig. 7 *B*, *iii* and *SI Appendix*, Fig. S16 *B*, *iii*). Albumin productions were 91% and 31% higher at the oxygen level of 13% (Fig. 7 *B*, *iv*) than those at the oxygen levels of 5% (Fig. 7 *A*, *iv*) and 20% (*SI Appendix*, Fig. S16 *B*, *iv*), respectively. The metabolic activities of the kidney microtissue confirmed that it favored the

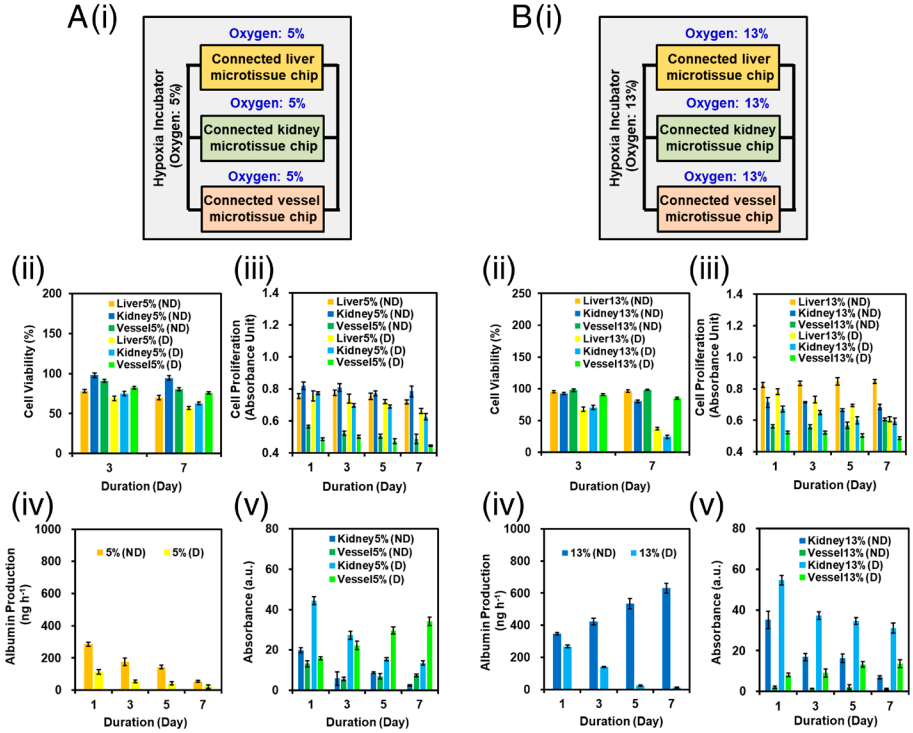

Fig. 7. Evaluations of oxygen effects on physiological activities and toxicity of APAP poisoning in three connected multiorgan-on-chips in a conventional hypoxia incubator. (*A*) (*i*) Schematic of the experimental design at the oxygen level of 5%. (*ii*) Live/dead assays, (*iii*) proliferation activities, and metabolic activities [(*iv*) albumin productions and (*v*) KIM-1 and ET-1 secretions] of the three connected multiorgan-on-chips in the presence of APAP poisoning (5 mmol L^{-1}) at the same oxygen level of 5% for all tissue types in connection. (*B*)(*i*) Schematic of the experimental design at the oxygen level of 13%. (*ii*) Live/dead assays, (*iii*) proliferation activities, and metabolic activities [(*iv*) albumin production and (*v*) KIM-1 and ET-1 secretions] of the three connected multiorgan-on-chips in the presence of APAP poisoning (5 mmol L^{-1}) at the same oxygen level of 13% for all tissue types in connection. "ND" indicates no drug (APAP), while "D" represents drug (n = 3).

oxygen level of 5%, while this level was not suitable for the liver and vessel microtissues (Fig. 7 *A*, *v*). Similarly, 13% of the oxygen level was favorable for the vessel microtissue (Fig. 7 *B*, *v*), and the oxygen level at 20% was not amenable to any of the three microtissues based on the metabolic activity assays (*SI Appendix*, Fig. S16 *B*, *iv* and *v*). The results clearly illustrated that the conventional hypoxia incubator-based approach could provide only one oxygen level during each experiment, where not all tissue types would be exposed to their optimal oxygen levels but only one or two at the maximum.

To investigate whether there was a difference in the mechanism of drug poisoning when the microtissues were cultured under different oxygen levels at 5%, 13%, and 20%, acetaminophen (APAP) (5 mmol L^{-1}) was separately applied to the conventional hypoxia incubator-, individual organ-on-a-chip-, and multiorgan-on-chips-based systems as described above. APAP is the most commonly used antipyretic and analgesic (53). When taken at therapeutic doses, it is considered a safe drug. Overdose can result in injuries of multiple organs, especially the liver and the kidney (54). The toxicity of APAP on the microtissues was first evaluated by the Live/Dead assay, the proliferation assay, and metabolic activity test in static culture and individual microtissue-on-a-chip systems separately. With APAP applied, substantial losses of viability in all the liver, kidney, and arterial vessel microtissues from Day 1 to 7 at all oxygen levels were observed. It is known that APAP is metabolically activated by the CYP enzymes to *N*-acetyl-p-benzoquinone imine, which is normally detoxified by glutathione (55). With APAP poisoning, the highest decreases in viability as well as proliferative and metabolic activities after the 7-d incubation were found in liver microtissues as compared with kidney and arterial vessel microtissues (*SI Appendix*, Figs. S5–S10). For example, after APAP poisoning at the overdose concentration of 5 mmol L^{-1} for 7 d, the viability decreases of the liver microtissues in the static and individual microtissue-on-a-chip cultures were 71% and 78%, respectively, at the optimal oxygen level of 13%, while the viability decreases of the kidney microtissues in the static and individual microtissue-on-a-chip cultures were 50% and 35%, respectively, at the optimal oxygen level of 5%, and those in the individual arterial vessel microtissue-on-a-chip culture were 15% and 21%, respectively, at the optimal oxygen level of 13% (*SI Appendix*, Figs. S5–S10 *B*, *i* and *ii*). Similar results were also found in proliferation and metabolic activity evaluations (*SI Appendix*, Figs. S5*B*–S10 *B*, *iii* and *iv*). Moreover, the toxicities of APAP poisoning on the vessel microtissue were lower than that on the liver and kidney microtissues, indicating that APAP was less toxic to the vessel than the liver at the dose assessed. These findings indicate that APAP poisoning on liver, kidney, and arterial vessel microtissues could be affected by oxygen levels.

APAP (5 mmol L^{-1}) was also applied to the closed-loop multiorgan-on-chips platform (Fig. 6). Fluorescence micrographs evidenced the effect of oxygen levels on APAP poisoning (Fig. 6 *A*, *ii*). Comparing the connected liver, kidney, and arterial vessel microtissue-on-chips, the APAP toxicity to the liver microtissue was 60%, which was 2.1- and 3.5-fold higher in viabilities than the APAP toxicity to the kidney and vessel microtissues on Day 7 (Fig. 6 *A*, *ii* and *iii*). The proliferation test demonstrated that APAP affected 1.1-fold and 1.5-fold higher in proliferation activities of the liver microtissue as compared to the activities of the kidney and arterial vessel microtissues (Fig. 6 *B*, *ii*). The oxygen effect on APAP toxicity was also clearly shown in the metabolic activity test. For example, albumin production decreased by 93% in the connected liver microtissue chip after the 7-d APAP poisoning at the oxygen level of 13%, while they decreased by 92% and 93% at the oxygen level of 5% and 20%, respectively (Fig. 6 *B*, *i* and *SI Appendix*, Figs. S12 *B*, *iv* and S13 B, *iv*). In contrast, the APAP toxicity to the liver microtissue was much lower at 5% and 20% in the hypoxia incubator as compared to that at the oxygen level of 13%. Therefore, the conventional hypoxia incubator-based multiorgan-on-chips system failed to clearly reflect drug metabolism within the connected culture.

The influence of oxygen level on the expressions of hypoxia and hyperoxia-induced genes was finally investigated. The mRNA levels of hypoxia-inducible factor-1α (HIF-1α), lactate dehydrogenase A (LDHA), and glucose transporter 1 (GLUT1) were measured in liver, kidney, and arterial vessel microtissues cultured at oxygen levels of 5%, 13%, and 20% in all the configurations

(Fig. 6 *C* and *SI Appendix*, Figs. S5–S10, S12, S13, and S17 and Table S1). HIF is a widely used marker for hypoxia (56). HIF-1α is ubiquitously expressed and can be rapidly degraded in the presence of oxygen by the von Hippel–Lindau ubiquitin pathway (57). When the oxygen level decreases below physiologic levels, HIF-1α does not undergo the initial hydroxylation required for the degradation, and protein levels increase (58). In the studies of the static culture, the HIF-1α-expression of the liver microtissue was at a higher level in the oxygen level at 5%, which was 15% and 5% higher as compared to 13% and 20% of oxygen, respectively, on Day 3. Compared to the oxygen level at 13% on Day 7, the expression of the HIF-1α was 21% higher than at the oxygen level at 20% (*SI Appendix*, Fig. S5 *C*, *i*). It is assumed that microtissues exposed to hyperoxic conditions would generate more reactive oxygen species by mitochondria (59). The oxidative stress may promote HIF-1α-induction (60). Together with the viability, proliferation, and metabolic activity assays, the results proved that the oxygen level at 13% was the most favorable for the liver microtissue among the three different oxygen levels. Similar results could also be observed in the liver microtissue-on-a-chip culture where the HIF-1α expressions were 26% and 21% higher at 5% and 20% than those at 13% of the oxygen levels on Day 7 (*SI Appendix*, Fig. S8 *C*, *i*). In addition, it was observed that the oxygen level affects the expressions of HIF-1α upon APAP poisoning in the developed liver microtissue-on-a-chip culture. For example, HIF-1α expression increased by 11%, 12%, and 8% on Day 1, while it increased to 13%, 18%, and 10% on Day 7 at the oxygen levels of 5%, 13%, and 20% after APAP poisoning, respectively (*SI Appendix*, Fig. S8 *C*, *i*). The oxygen effects on HIF-1α expressions in the multiorgan-on-chips platform were also evaluated (Fig. 6 *C*, *i*). The expressions of HIF-1α showed the lowest level in the connected liver microtissue-on-a-chip and the connected kidney microtissue-on-a-chip when exposed to 13% of the oxygen level as compared to the counterparts at oxygen levels of 5% and 20%, while the lowest level in the kidney microtissue-on-a-chip was at 5%.

The LDHA level is closely related to glucose metabolism, which can reduce pyruvate to lactate (61). This process allows glycolysis to proceed in an anoxic condition. Among the lactate dehydrogenase protein subunits, LDHA has been associated with oxygen levels (62). As the oxygen levels varied at 5%, 13%, and 20%, the LDHA expressions after APAP poisoning were different. As shown in Fig. 6 *C*, *ii*, the lowest expression of LDHA was found at the oxygen level of 5% as compared to 13% and 20% in the connected kidney microtissue-on-a-chip. This observation indicated that lower oxygen contents would be the more relevant oxygen levels for the cultured kidney microtissues, while the 13% and 20% oxygen levels are generally high for the kidney microtissue. The applied oxygen levels could affect the kidney microtissue responses to APAP poisoning, with oxygen level at 5% delaying the microtissue death. In addition, the expression of LDHA was lower when the liver microtissues were exposed under 13% of the oxygen condition than hypoxia and hyperoxia. APAP poisoning enhanced the expressions of HIF-1α and LDHA at all oxygen levels. GLUT1 is the most studied subtype for basal glucose uptake (63). Furthermore, GLUT1 is directly responsible for glucose metabolism and is commonly up-regulated by both HIF-1α and HIF-2α (63). GLUT1 was selected as an indirect biomarker of HIF-1 function. It was shown that the lowest expressions of GLUT1 occurred at 5% in the connected kidney microtissue-on-a-chip and at 13% in the connected liver microtissue-on-a-chip and arterial vessel microtissue-on-a-chip cultures (Fig. 6 *C*, *iii*). The expressions of HIF-1α, LDHA, and GLUT1 in the connected kidney microtissue-on-a-chip revealed similar trends as those in the connected liver and arterial vessel microtissue-on-chips. Therefore, it can be concluded that the oxygen level affects the expressions of HIF-1α, LDHA, and GLUT1 in the liver, kidney, and arterial vessel microtissues. Together with cell viability as well as proliferation and metabolic activity tests, the results again proved that the oxygen level at 13% would be the most favorable for liver and vessel microtissues and the kidney microtissues would be more amenable to survive at 5% among the three different oxygen levels. To conclude, the developed closed-loop modular multiorgan-on-chips platform could not only enable individual culture of multiple microtissues at their respective physiological oxygen microenvironments but also be used for studies on oxygen-induced drug metabolism.

Discussion

We have developed an automated closed-loop multiorgan-on-chips platform that used a modular design of microfluidic thermoplastic chips to ensure an oxygen-impermeable microenvironment in the flowing medium for independently controlling and monitoring the dissolved oxygen levels. All of the oxygen-controlling and monitoring were performed in a real-time and automated manner, allowing for self-sustaining investigations of drug-induced organ responses in the (multi)organ-on-a-chip(s) platform with the drug poisoning for up to a 7-d culture period evaluated. The biological studies revealed that the developed platform could indeed independently provide physiological oxygen levels in the flowing culture medium that enabled the investigation of drug metabolism. It is believed that our automated closed-loop modular (multi)organ-on-a-chip platform integrated with the controlling and real-time monitoring modules would be compatible with existing organ-on-a-chip models and possibly promote their performances in drug screening by providing more physiologically relevant oxygen levels.

This study is an investigation on dynamically culturing different microtissues (e.g., liver/kidney/arterial vessel) hosted in a single fluidic platform with the capacity to individually tune the oxygen levels within individual bioreactors. Nevertheless, there exist several potential areas for improvements of the current automated closed-loop modular organ-on-a-chip platform. First, the current developed platform could independently control the physiological oxygen level in the range of 4 to 20%, which were suitable for microtissues such as the liver, kidney, and arterial vessel that we demonstrated and beyond. As the platform will be applied for other microtissue types that feature even lower physiological oxygen levels (e.g., 0.5 to 4%), the oxygen scavenger could be redesigned by increasing the microchannel length, scavenging solution concentration, and scavenging flow rate to further reach these concentrations. Second, the metabolic activities and biomarker levels were not measured in situ, which may lead to contamination during the resealing process. These measurements usually require multiple steps and large working volumes that hinder in situ detection. Further real-time bioanalytical measurements of microtissues integrated with the closed-loop multiorgan-on-chips system remain an unmet need (10, 64). To this end, connected microchannels and microvalves could be integrated in the bioreactors in combination with biosensing units. Third, in addition to controlling and monitoring oxygen levels in the platform, the other physical parameters, such as pH value and temperature could also be controlled and monitored (10, 65). Fourth, the bonding between the dissimilar PMMA and PDMS surfaces may be enhanced to promote chip reliability and reduce potential leakage (66). Fifth, in the current design, the three different microtissue-on-chips were parallelly connected, and they failed to reproduce the natural interactions across multiple tissues. Moreover, scaling of

paracrine communications and selective transport of drugs should be considered to improve the fidelity of the multiorgan-on-chips platform on drug development (67). The volume of the applied culture medium for the entire system in our demonstrations was substantial, which would diminish the paracrine effects due to extreme dilutions. Further developments will be investigated toward miniaturizing and reconfiguring the platform designs, therefore enabling accurate paracrine interactions among the multiple organ types. Nevertheless, we have shown at the initial prototyping stage that, such an automated platform validated the feasibility of integrating self-sustaining and tightly controlled oxygen-generation and scavenging modules, and the proof-of-concept studies on drug screening. Additional efforts will be invested to improvement of the platform design that allows for true multiorgan interactions and applications of the developed platform to systematic understanding of its broad utility, for eventually constructing more physiologically and pathologically relevant in vitro human-based microtissue models.

Materials and Methods

Raw-cast transparent and black PMMA sheets were used to fabricate the microfluidic chips. The bioreactor was assembled in a resealable manner to allow for the opening and closing of the system for subsequent biological assays when necessary. For fabrication of the oxygen scavenger, open microchannels were ablated on the two pieces of PMMA chips. Subsequently, a PDMS membrane was fabricated by spin coating. The PDMS membrane was then sandwiched between two pieces of PMMA chips and sealed under thermal treatment in a vacuum oven at 50 °C and −30 psi for 2 h. The inlet and outlet were connected to the main microchannel, while the inlet of the bottom microchannel was connected with $Na_2SO_3/CoSO_4$ solution integrated with the syringe pump. For fabrication of the mixer, microchannels in the PMMA chips were created by laser ablation and were sealed by thermal treatment. For fabrication of the oxygen generator, an open-channeled PDMS microfluidic chip was fabricated by a photolithography technique. The microchannels were sealed by a PDMS membrane, which were sandwiched between PMMA chips. A closed-loop modular organ-on-a-chip platform was integrated by a Teflon tubing or a Tygon microbore tubing. All the connections were sealed by epoxy.

Materials and methods are further expanded in *SI Appendix*, which include Materials used for the experiments, Chip fabrication for use producing the oxygen generators and oxygen scavengers, Biosensor fabrication for measuring oxygen levels, Integration of the full operational system, Cell culture, Cell encapsulation within GelMA hydrogel dots, Hypoxia incubator experiments, Microtissue viability, proliferation, and functionality, Quantitative PCR assessments of gene expressions, and Simulating oxygen consumption of the microtissue models.

Data, Materials, and Software Availability. All study data are included in the article and/or *SI Appendix*.

ACKNOWLEDGMENTS. Support from the NIH (R21EB025270, R21HL168656, R00CA201603, R01EB028143, UG3TR003274, UH3TR003274, UH3TR003274-S1, R01HL153857, R01HL166522, and R01CA282451), the NSF (CBET-EBMS-1936105 and CISE-IIS-2225698), the Chan Zuckerberg Initiative (2022-316712), and the Brigham Research Institute is acknowledged. We further thank Praveen Bandaru and Carolina Parra-Cantu for initial help with chip fabrications and discussions.

Author affiliations: [a]Division of Biomedical Engineering, Department of Medicine, Brigham and Women's Hospital, Harvard Medical School, Boston, MA 02139; [b]Department of Physics, School of Engineering and Applied Sciences, Harvard University, Cambridge, MA 02138; [c]Wallace H. Coulter Department of Biomedical Engineering, Georgia Institute of Technology, Atlanta, GA 30318; [d]Division of Cardiovascular Medicine, Department of Medicine, Brigham and Women's Hospital, Harvard Medical School, Boston, MA 02115; [e]Harvard Stem Cell Institute, Harvard University, Cambridge, MA 02138; and [f]Broad Institute of Massachusetts Institute of Technology (MIT) and Harvard, Cambridge, MA 02142

Author contributions: N.J., G.Y., and Y.S.Z. designed research; N.J., G.Y., Y.Y., J.G., J.L., A.V.P., A.G., B.A.G.d.M., F.L.M., M.G., M.P., N.C., and C.E.G.-M. performed research; G.-A.K., S.T., and M.D.G.-H. contributed new reagents/analytic tools; N.J., G.Y., Y.Y., and J.G. analyzed data; J.L. designed the user interface; M.G. contributed to drawings; Y.S.Z. supervised the project; and N.J., G.Y., and Y.S.Z. wrote the paper.

Competing interest statement: Y.S.Z. sits on the scientificadvisory board and holds options of Xellar, neither of which however, participated in or bias the work.

1. N. T. Elliott, F. Yuan, A review of three-dimensional in vitro tissue models for drug discovery and transport studies. *J. Pharm. Sci.* **100**, 59–74 (2011).
2. O. F. Vila, Y. Qu, G. Vunjak-Novakovic, In vitro models of neuromuscular junctions and their potential for novel drug discovery and development. *Expert. Opin. Drug. Discov.* **15**, 307–317 (2020).
3. S. A. Langhans, Three-dimensional in vitro cell culture models in drug discovery and drug repositioning. *Front. Pharmacol.* **9**, 6 (2018).
4. K.-H. Nam, A. S. T. Smith, S. Lone, S. Kwon, D.-H. Kim, Biomimetic 3D tissue models for advanced high-throughput drug screening. *J. Lab. Autom.* **20**, 201–215 (2015).
5. S. Breslin, L. O'Driscoll, Three-dimensional cell culture: The missing link in drug discovery. *Drug Discov. Today* **18**, 240–249 (2013).
6. M.-H. Wu, S.-B. Huang, G.-B. Lee, Microfluidic cell culture systems for drug research. *Lab Chip* **10**, 939–956 (2010).
7. B. Zhang, A. Korolj, B. F. L. Lai, M. Radisic, Advances in organ-on-a-chip engineering. *Nat. Rev. Mater.* **3**, 257–278 (2018).
8. S. N. Bhatia, D. E. Ingber, Microfluidic organs-on-chips. *Nat. Biotechnol.* **32**, 760–772 (2014).
9. C. Moraes, G. Mehta, S. C. Lesher-Perez, S. Takayama, Organs-on-a-chip: A focus on compartmentalized microdevices. *Ann. Biomed. Eng.* **40**, 1211–1227 (2012).
10. Y. S. Zhang *et al.*, Multisensor-integrated organs-on-chips platform for automated and continual in situ monitoring of organoid behaviors. *Proc. Natl. Acad. Sci. U.S.A.* **114**, E2293–E2302 (2017).
11. J. D. Caplin, N. G. Granados, M. R. James, R. Montazami, N. Hashemi, Microfluidic organ-on-a-chip technology for advancement of drug development and toxicology. *Adv. Healthc. Mater.* **4**, 1426–1450 (2015).
12. C. Ma, Y. Peng, H. Li, W. Chen, Organ-on-a-chip: A new paradigm for drug development. *Trends Pharmacol. Sci.* **42**, 119–133 (2020).
13. M. C. Brahimi-Horn, J. Pouysségur, Oxygen, a source of life and stress. *FEBS Lett.* **581**, 3582–3591 (2007).
14. A. Mohyeldin, T. Garzón-Muvdi, A. Quiñones-Hinojosa, Oxygen in stem cell biology: A critical component of the stem cell niche. *Cell Stem Cell* **7**, 150–161 (2010).
15. C.-C. Wang, K.-M. Fang, C.-S. Yang, S.-F. Tzeng, Reactive oxygen species-induced cell death of rat primary astrocytes through mitochondria-mediated mechanism. *J. Cell Biochem.* **107**, 933–943 (2009).
16. S. Orrenius, Reactive oxygen species in mitochondria-mediated cell death. *Drug Metab. Rev.* **39**, 443–455 (2007).
17. D. M. Panchision, The role of oxygen in regulating neural stem cells in development and disease. *J. Cell Physiol.* **220**, 562–568 (2009).
18. L. Packer, K. Fuehr, Low oxygen concentration extends the lifespan of cultured human diploid cells. *Nature* **267**, 423–425 (1977).
19. V. Palacio-Castañeda, L. Kooijman, B. Venzac, W. P. R. Verdurmen, S. Le Gac, Metabolic switching of tumor cells under hypoxic conditions in a tumor-on-a-chip model. *Micromachines* **11**, 382 (2020).
20. C. Reinke, S. Bevans-Fonti, L. F. Drager, M.-K. Shin, V. Y. Polotsky, Effects of different acute hypoxic regimens on tissue oxygen profiles and metabolic outcomes. *J. Appl. Physiol.* **111**, 881–890 (2011).
21. S. J. Kierans, C. T. Taylor, Regulation of glycolysis by the hypoxia-inducible factor (HIF): Implications for cellular physiology. *J. Appl. Physiol.* **599**, 23 (2021).
22. W. K. R. Barnikol, H. Pötzschke, A novel, non-invasive diagnostic clinical procedure for the determination of an oxygenation status of chronic lower leg ulcers using peri-ulceral transcutaneous oxygen partial pressure measurements: Results of its application in chronic venous insufficiency (CVI). *Ger. Med. Sci.* **10**, Doc11 (2012).
23. Z. Ivanovic, Hypoxia or in situ normoxia: The stem cell paradigm. *J. Cell Physiol.* **219**, 271–275 (2009).
24. S. G. Kim *et al.*, Bilirubin activates transcription of HIF-1α in human proximal tubular cells cultured in the physiologic oxygen content. *J. Korean Med. Sci.* **29**, S146–S154 (2014).
25. M. D. Brennan, M. L. Rexius-Hall, L. J. Elgass, D. T. Eddington, Oxygen control with microfluidics. *Lab Chip* **14**, 4305–4318 (2014).
26. G. D'Ippolito, S. Diabira, G. A. Howard, B. A. Roos, P. C. Schiller, Low oxygen tension inhibits osteogenic differentiation and enhances stemness of human MIAMI cells. *Bone* **39**, 513–522 (2006).
27. H. Kappus, H. Sies, Toxic drug effects associated with oxygen metabolism: Redox cycling and lipid peroxidation. *Experientia* **37**, 1233–1241 (1981).
28. Anonymous, Noninvasive oxygen monitoring in three-dimensional tissue cultures under static and dynamic culture conditions. *Biores. Open Access* **4**, 266–277 (2015).
29. R. Wang, F. Jin, H. Zhong, A novel experimental hypoxia chamber for cell culture. *Am. J. Cancer Res.* **4**, 53–60 (2014).
30. Y. B. Kang, J. Eo, B. Bulutoglu, M. L. Yarmush, O. B. Usta, Progressive hypoxia-on-a-chip: An in vitro oxygen gradient model for capturing the effects of hypoxia on primary hepatocytes in health and disease. *Biotechnol. Bioeng.* **117**, 763–775 (2020).
31. Y.-A. Chen *et al.*, Generation of oxygen gradients in microfluidic devices for cell culture using spatially confined chemical reactions. *Lab Chip* **11**, 3626–3633 (2011).
32. E. J. Park, K. R. Reid, W. Tang, R. T. Kennedy, R. Kopelman, Ratiometric fiber optic sensors for the detection of inter- and intra-cellular dissolved oxygen. *J. Mater. Chem.* **15**, 2913–2919 (2005).
33. S. G. Charati, S. A. Stern, Diffusion of gases in silicone polymers: Molecular dynamics simulations. *Macromolecules* **31**, 5529–5535 (1998).
34. S. Hitoshi *et al.*, Oxygen permeability of surface-modified poly(dimethylsiloxane) characterized by scanning electrochemical microscopy. *Chem. Lett.* **35**, 234–235 (2006).

35. W.-H. Yang, V. F. Smolen, N. A. Peppas, Oxygen permeability coefficients of polymers for hard and soft contact lens applications. *J. Membr. Sci.* **9**, 53–67 (1981).
36. A. Pourmand *et al.*, Fabrication of whole-thermoplastic normally closed microvalve, micro check valve, and micropump. *Sens. Actuators B Chem.* **262**, 625–636 (2018).
37. N. S. Bhise *et al.*, A liver-on-a-chip platform with bioprinted hepatic spheroids. *Biofabrication* **8**, 014101 (2016).
38. B. Jiang *et al.*, Sodium sulfite is a potential hypoxia inducer that mimics hypoxic stress in Caenorhabditis elegans. *J. Biol. Inorg. Chem.* **16**, 267–274 (2011).
39. M. Skolimowski *et al.*, Microfluidic dissolved oxygen gradient generator biochip as a useful tool in bacterial biofilm studies. *Lab Chip* **10**, 2162–2169 (2010).
40. A. D. Stroock *et al.*, Chaotic mixer for microchannels. *Science* **295**, 647–651 (2002).
41. H. Remmer, The role of the liver in drug metabolism. *Am. J. Med.* **49**, 617–629 (1970).
42. J. R. Derrick, D. Russell, Oxygen tensions in tissues. *Arch. Surg.* **88**, 1059–1062 (1964).
43. K. Wrzesinski *et al.*, HepG2/C3A 3D spheroids exhibit stable physiological functionality for at least 24 days after recovering from trypsinisation. *Toxicol. Res.* **2**, 163–172 (2013).
44. G. Sabbioni, R. J. Turesky, Biomonitoring human albumin adducts: The past, the present, and the future. *Chem. Res. Toxicol.* **30**, 332–366 (2017).
45. A. N. Friedman, S. Z. Fadem, Reassessment of albumin as a nutritional marker in kidney disease. *J. Am. Soc. Nephrol.* **21**, 223–230 (2010).
46. N. Chen, K. Aleksa, C. Woodland, M. Rieder, G. Koren, Ontogeny of drug elimination by the human kidney. *Pediatr. Nephrol.* **21**, 160–168 (2006).
47. M. J. Ryan *et al.*, HK-2: An immortalized proximal tubule epithelial cell line from normal adult human kidney. *Kidney Int.* **45**, 48–57 (1994).
48. C. Yin, N. Wang, Kidney injury molecule-1 in kidney disease. *Ren. Fail.* **38**, 1567–1573 (2016).
49. C. Betsholtz, Cell–cell signaling in blood vessel development and function. *EMBO Mol. Med.* **10**, e8610 (2018).
50. M. Iglarz, M. Clozel, Mechanisms of ET-1-induced endothelial dysfunction. *J. Cardiovasc. Pharmacol.* **50**, 621–628 (2007).
51. S. H. Lee, S. I. Do, H. S. Kim, Hyperoxia accelerates progression of hepatic fibrosis by up-regulation of transforming growth factor-β expression. *World J. Gastroenterol.* **20**, 3011–3017 (2014).
52. T. Kietzmann, Metabolic zonation of the liver: The oxygen gradient revisited. *Redox Biol.* **11**, 622–630 (2017).
53. H. S. Smith, Potential analgesic mechanisms of acetaminophen. *Pain Phys.* **12**, 269–280 (2009).
54. T. D. Boyer, S. L. Rouff, Acetaminophen-induced hepatic necrosis and renal failure. *JAMA* **218**, 440–441 (1971).
55. E. Leclerc *et al.*, Investigation of acetaminophen toxicity in HepG2/C3a microscale cultures using a system biology model of glutathione depletion. *Cell Biol. Toxicol.* **31**, 173–185 (2015).
56. S. J. Welsh, G. Powis, Hypoxia inducible factor as a cancer drug target. *Curr. Cancer Drug Targets* **3**, 391–405 (2003).
57. G. L. Semenza, Hydroxylation of HIF-1: Oxygen sensing at the molecular level. *Physiology* **19**, 176–182 (2004).
58. B. H. Jiang, G. L. Semenza, C. Bauer, H. H. Marti, Hypoxia-inducible factor 1 levels vary exponentially over a physiologically relevant range of O2 tension. *Am. J. Physiol. Cell Physiol.* **271**, C1172–C1180 (1996).
59. A. J. Kowaltowski, N. C. de Souza-Pinto, R. F. Castilho, A. E. Vercesi, Mitochondria and reactive oxygen species. *Free Radic. Biol. Med.* **47**, 333–343 (2009).
60. N. Gao *et al.*, Vanadate-induced expression of hypoxia-inducible factor 1α and vascular endothelial growth factor through phosphatidylinositol 3-kinase/Akt pathway and reactive oxygen species. *J. Biol. Chem.* **277**, 31963–31971 (2002).
61. W. Cui, F. Wu, L. Ma, Hypoxia associated biomarkers in lung cancer-An update. *Eur. Rev. Med. Pharmacol. Sci.* **21**, 43–46 (2017).
62. B. S. Sørensen *et al.*, Influence of oxygen concentration and pH on expression of hypoxia induced genes. *Radiother. Oncol.* **76**, 187–193 (2005).
63. M. B. Calvo, A. Figueroa, E. G. Pulido, R. G. Campelo, L. A. Aparicio, Potential role of sugar transporters in cancer and their relationship with anticancer therapy. *Int. J. Endocrinol.* **2010**, 205357 (2010).
64. J. Aleman, T. Kilic, L. S. Mille, S. R. Shin, Y. S. Zhang, Microfluidic integration of regeneratable electrochemical affinity-based biosensors for continual monitoring of organ-on-a-chip devices. *Nat. Protoc.* **16**, 2564–2593 (2021).
65. S. A. Mousavi Shaegh *et al.*, A microfluidic optical platform for real-time monitoring of pH and oxygen in microfluidic bioreactors and organ-on-chip devices. *Biomicrofluidics* **10**, 044111 (2016).
66. H. Yuk, T. Zhang, G. A. Parada, X. Liu, X. Zhao, Skin-inspired hydrogel–elastomer hybrids with robust interfaces and functional microstructures. *Nat. Commun.* **7**, 12028 (2016).
67. J. P. Wikswo *et al.*, Scaling and systems biology for integrating multiple organs-on-a-chip. *Lab Chip* **13**, 3496–3511 (2013).